CRYSTAL GROWTH & DESIGN

pubs.acs.org/crystal

Article

Shaping Tin Nanocomposites through Transient Local Conversion Reactions

Hans C. Hendrikse, Stivell Hémon-Charles, Lukas Helmbrecht, Eliane P. van Dam, Erik C. Garnett, and Willem L. Noorduin*

Cite This: https://doi.org/10.1021/acs.cgd.1c00393

Read Online

ACCESS | Metrics & More | Article Recommendations | Supporting Information

ABSTRACT: Shape-preserving conversion offers a promising strategy to transform self-assembled structures into advanced functional components with customizable composition and shape. Specifically, the assembly of barium carbonate nanocrystals and amorphous silica nanocomposites ($BaCO_3/SiO_2$) offers a plethora of programmable three-dimensional (3D) microscopic geometries, and the nanocrystals can subsequently be converted into functional chemical compositions, while preserving the original 3D geometry. Despite this progress, the scope of these conversion reactions has been limited by the requirement to form carbonate salts. Here, we overcome this limitation using a single-step cation/anion exchange that is driven by the temporal pH change at the converting nanocomposite. We demonstrate the proof of principle by converting $BaCO_3/SiO_2$ nanocomposites into tin-containing nanocomposites, a metal without a stable carbonate. We find that $BaCO_3/SiO_2$ nanocomposites convert in a single step into hydroromarchite nanocomposites ($Sn_3(OH)_2O_2/SiO_2$) with excellent preservation of the 3D geometry and fine features. We explore the versatility and tunability of these $Sn_3(OH)_2O_2/SiO_2$ nanocomposites as a precursor for functional compositions by developing shape-preserving conversion routes to two desirable compositions: tin perovskites ($CH_3NH_3SnX_3$, with X = I or Br) with tunable photoluminescence (PL) and cassiterite (SnO_2)—a widely used transparent conductor. Ultimately, these findings may enable integration of functional chemical compositions into advanced morphologies for next-generation optoelectronic devices.

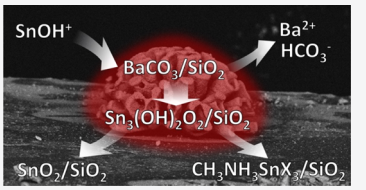

Bioinspired strategies offer tremendous opportunities for ordering building blocks across multiple length scales into advanced functional materials.[1−14] The coprecipitation of metal carbonate nanocrystals (MCO_3, with M = Ba^{2+}, Sr^{2+}, or Ca^{2+}) and amorphous silica (SiO_2) offers an ideal system to explore this potential, as their co-assembly yields highly intricate, yet easily controllable 3D nanocomposite shapes also known as biomorphs.[15−26] Rational modulation of the reaction conditions (pH, CO_2 concentration, temperature, etc.) enables steering of the assembly toward a wide diversity of shapes (e.g., coral, vase, and helix forms) that can be further patterned and hierarchically organized.

Although the initial self-assembly process constrains the nanocrystals' chemical composition to metal carbonate salts, post-assembly procedures have been developed to overcome this limitation. For example, microhelices have been decorated with magnetite mesocrystals, and silane chemistry enables chemical functionalization of the nanocomposites' silica matrix.[27,28] Alternatively, shape-preserving conversion reactions allow for complete conversion of the $BaCO_3$ nanocrystals into a wide selection of lead perovskites and metal chalcogenides with desirable optical, electronic, and chemical properties, while inheriting the 3D shape and fine features of the original nanocomposite.[29,30] These conversions are achieved by sequential series of cation and anion exchange reactions. Here, excellent chemical conversion and shape preservation are achieved because the high surface-to-volume ratio of the $BaCO_3$ nanocrystals makes them prone to conversion, while the surrounding silica matrix provides mechanical support needed for shape preservation. Although many different chemical compositions have been achieved in this way, all of these conversions require the formation of a carbonate intermediate. Because many interesting compounds do not form a metal carbonate, this limits the choice of accessible chemical compositions for furnishing nanocomposites with advanced functionalities.

The mechanistic details of conversion reactions may offer inspiration for overcoming this challenge. From a thermodynamic perspective, the viability of exchange reactions can be rationalized by the difference in formation energy of the forming and disappearing salt and the reduction potential of the involved ions.[31,32] This rationalization is usually complemented by considerations of the in situ reaction conditions during transformation, as it is well known that the local chemistry plays a major role in this process.[32−34] Especially the reaction conditions near the solid−liquid interface, the so-called reaction zone, are important and can be entirely different from the bulk solution. We hypothesize

Received: April 6, 2021
Revised: July 2, 2021

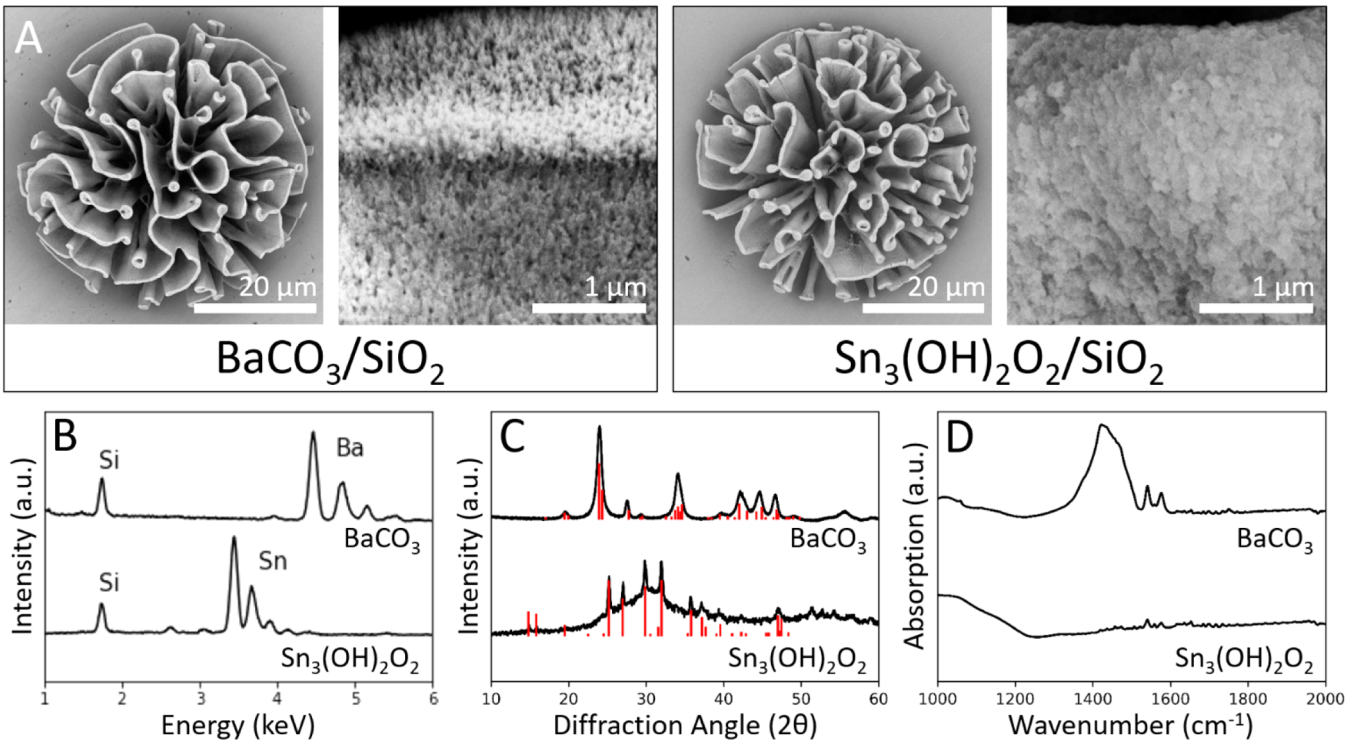

Figure 1. Conversion from $BaCO_3/SiO_2$ to $Sn_3(OH)_2O_2/SiO_2$ nanocomposites. (A) SEM images of (different) nanocomposites before (left) and after (right) conversion, showing that the coral-like shape is retained despite significant changes to the nanocrystal morphology (see respective close-up SEM images). (B) EDS measurements of nanocomposites before (top) and after (bottom) conversion, indicating full replacement of barium with tin. (C) XRD characterization showing the conversion of $BaCO_3$ to $Sn_3(OH)_2O_2$ (red lines indicate reference peaks). (D) IR spectrum showing the disappearance of the fingerprint peak of a carbonate anion at ~1450 cm^{-1} after conversion to $Sn_3(OH)_2O_2$.

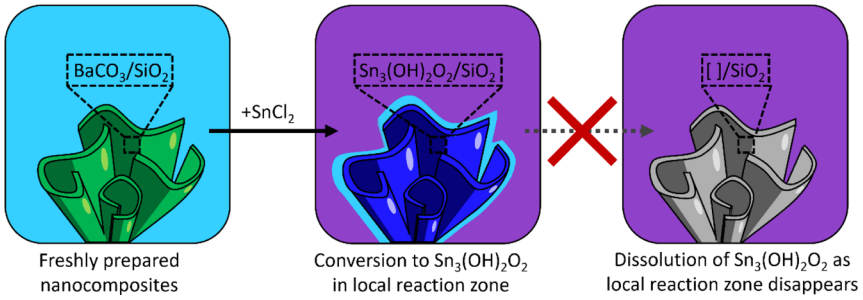

Figure 2. Proposed conversion mechanism of $BaCO_3$ to $Sn_3(OH)_2O_2$ in nanocomposites. Sn^{2+} hydrolysis decreases the pH of water (I). High pH is indicated by light blue (left) and low pH is indicated by purple (middle, right). Locally, the pH increases again by dissolving $BaCO_3$ (II, middle, indicated by light blue around the nanocomposite), which causes $Sn_3(OH)_2O_2$ to precipitate (III). Once all $BaCO_3$ is dissolved, the local pH decreases to the bulk pH, thereby initiating dissolution of $Sn_3(OH)_2O_2$ (right, IV).

that the temporary local concentration gradients in the reaction zone may offer new reaction mechanisms for previously impossible conversion reactions.

In this article, we demonstrate that chemical gradients in the local reaction zone enable conversion of barium carbonate nanocomposites ($BaCO_3/SiO_2$) into a selection of tin-containing nanocomposites. A straightforward cation exchange is not possible in this conversion, as tin does not form a stable carbonate salt.[35] However, we find that the transient local conversion conditions, along with the poor solubility of tin in water, result in a concurrent cation/anion exchange toward hydroromarchite ($Sn_3(OH)_2O_2$). Meanwhile, the inert silica maintains the macroscopic shape and fine details of the original nanocomposite, as previously demonstrated.[29,30] Furthermore, we explore the versatility and tunability of these $Sn_3(OH)_2O_2/SiO_2$ nanocomposites as precursors for functional compositions by developing shape-preserving conversion routes to two desirable compositions: transparent, conducting cassiterite (SnO_2), and semiconducting tin perovskite ($CH_3NH_3SnX_3$, with X = I or Br).[36−43] Hence, by demonstrating this conversion mechanism, we open up pathways to new functional materials with controllable shapes.

RESULTS AND DISCUSSION

We study the ion exchange to tin from $BaCO_3/SiO_2$ coral-shaped nanocomposites. We assemble $BaCO_3/SiO_2$ coral shapes following previously reported procedures.[22] Subsequently, these coral shapes are immersed in an aqueous solution of 100 mM $SnCl_2$ under a nitrogen atmosphere (see Supporting Information for details). Within 30 s of immersion, the barium ions in the nanocomposites are completely replaced by tin according to energy-dispersive X-ray spectroscopy (EDS,

https://doi.org/10.1021/acs.cgd.1c00393
Cryst. Growth Des. XXXX, XXX, XXX−XXX

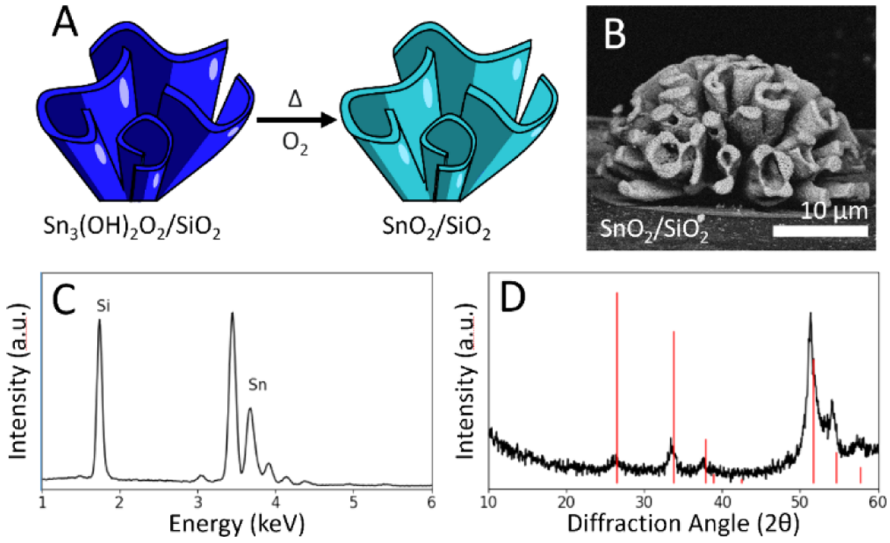

Figure 3. Conversion of $Sn_3(OH)_2O_2$ to the SnO_2 nanocomposite. (A) Schematic representation of the conversion from $Sn_3(OH)_2O_2$ to SnO_2. (B) SEM of the resulting SnO_2/SiO_2 nanocomposites, showing preservation of the coral-like shape. (C) EDS and (D) XRD confirming complete conversion to SnO_2 (red lines indicate SnO_2 reference peaks).

Figure 1B). Furthermore, scanning electron microscopy (SEM) shows excellent shape preservation with sub-micrometer fidelity, despite significant changes to the nanocrystal morphology (Figure 1A).

Remarkably, X-ray diffraction (XRD, Figure 1C) reveals that the nanocrystals inside the nanocomposites are composed of hydroromarchite ($Sn_3(OH)_2O_2$) with an average grain size of 33 nm (see Supporting Information).[44,45] Thus, besides the barium cations being replaced for tin, the carbonate anions are also substituted with oxyhydroxide. Infrared spectroscopy (IR) confirms that the characteristic carbonate fingerprint peak (~1450 cm^{-1}) of $BaCO_3$ disappears after the conversion (Figure 1D). Hence, both cations and anions are replaced in a single step during this shape-preserving chemical conversion.

We hypothesize that during the concurrent shape-preserving cation/anion exchange, a cascade of reactions occurs (Figure 2). First, in the bulk solution, the following reaction occurs[46,47]

$$Sn^{2+}(aq) + H_2O(l) \rightarrow Sn(OH)^+(aq) + H^+(aq) \quad (I)$$

Here, tin ions hydrolyze in water, forming $SnOH^+$ and acid (I), which is consistent with an observed decrease in the pH from 7.0 to 2.0. This acidic solution leads to the dissolution of $BaCO_3$ nanocrystals in the nanocomposite and thereby locally increases the pH in the close vicinity of the nanocomposite (II)

$$BaCO_3(s) + 2H^+(aq) \rightarrow Ba^{2+}(aq) + H_2O + CO_2(aq) \quad (II)$$

This increased local pH, combined with the high tin concentration in the solution, results in the formation of the desired $Sn_3(OH)_2O_2$ (III)[46,48]

$$3Sn(OH)^+(aq) + H_2O(l) \rightarrow Sn_3(OH)_2O_2(s) + 3H^+(l) \quad (III)$$

Consistent with this mechanism, deliberately increasing the pH of the bulk solution to 13−14 by adding a base (1.0 M NaOH) results in precipitation of $Sn_3(OH)_2O_2$ in the entire solution via III (see Supporting Information).[49]

Allowing the conversion to continue after the formation of the desired $Sn_3(OH)_2O_2$ results in an undesired reaction IV, which causes the dissolution of the nanocrystals

$$Sn_3(OH)_2O_2(s) + 3H^+(aq) \rightarrow 2Sn(OH)^+(aq) + H_2O(l) \quad (IV)$$

This reaction occurs once all $BaCO_3$ is dissolved and the local pH decreases to the acidic pH of the bulk solution. Due to this, $Sn_3(OH)_2O_2$ in the nanocomposites dissolves as it is only stable at a pH above 3.5 (bulk pH = 2.0),[47] leaving the empty silica scaffold behind (see Supporting Information). Thus, the suggested mechanism indicates that preservation of the local reaction zone is essential for the conversion.

The importance of this local reaction zone can be demonstrated by simply disturbing the experiment. Already gently stirring the reaction solution or shaking the substrate disturbs the local gradients, resulting in either incomplete conversion or depletion of the nanocomposite. Collectively, these experiments suggest that dissolution of $BaCO_3$ creates a local transient reaction zone that enables the precipitation of $Sn_3(OH)_2O_2$ in the nanocomposite with preservation of the original 3D shape.

This shape-preservation reaction to $Sn_3(OH)_2O_2/SiO_2$ nanocomposites opens up opportunities for developing further conversion pathways toward shape-controlled 3D morphologies with desirable tin compositions. We explore this potential for the conversion of $Sn_3(OH)_2O_2$ to tin dioxide (cassiterite, SnO_2). SnO_2-based materials are widely used for optoelectronic and battery applications, where shape-controlled 3D morphologies could offer new and improved functionalities.[36−39] Previous studies have already shown that $Sn_3(OH)_2O_2$ crystals can be converted into SnO_2 via dehydration and subsequent oxidation as follows[50−52]

$$Sn_3O_2(OH)_2(s) \rightarrow 3SnO(s) + H_2O(g) \quad (V)$$

$$2SnO(s) + O_2(g) \rightarrow 2SnO_2(s) \quad (VI)$$

So far, these reactions have only been performed on bulk crystals where the initial shape preservation was lost during conversion,[50] as the mechanical stress during the dehydration

https://doi.org/10.1021/acs.cgd.1c00393
Cryst. Growth Des. XXXX, XXX, XXX−XXX

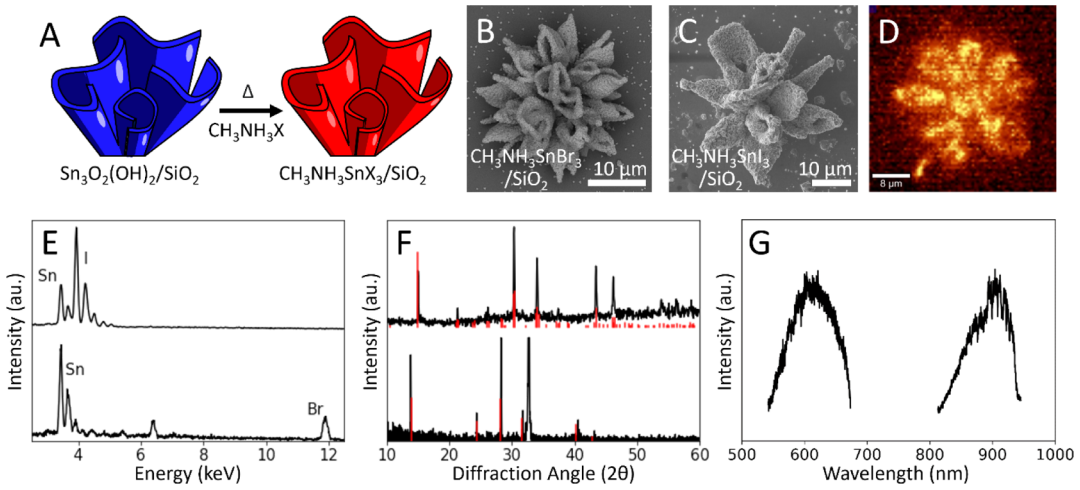

Figure 4. Conversion of $Sn_3(OH)_2O_2/SiO_2$ to $CH_3NH_3SnX_3/SiO_2$ nanocomposites with X = Br^- and I^-. (A) Schematic representation of the conversion from $Sn_3(OH)_2O_2/SiO_2$ to $CH_3NH_3SnX_3/SiO_2$ nanocomposites, which occurs at elevated temperatures when CH_3NH_3X is added. (B) SEM of a $CH_3NH_3SnBr_3/SiO_2$ nanocomposite. (C) SEM of a $CH_3NH_3SnI_3/SiO_2$ nanocomposite. (D) PL intensity map of a $CH_3NH_3SnBr_3/SiO_2$ nanocomposite at 610 nm showing emission from the nanocomposite exclusively. Lighter color indicates higher intensity. (E) EDS and (F) XRD analyses of coral-like nanocomposites containing $CH_3NH_3SnBr_3$ (top) and $CH_3NH_3SnI_3$ (bottom). (G) PL spectrum of $CH_3NH_3SnBr_3/SiO_2$ (at 610 nm) and $CH_3NH_3SnI_3/SiO_2$ nanocomposites (at 880 nm).

and oxidation processes destroys the morphology of the original crystal. In contrast, ion-exchange reactions on nanocomposites do enable shape preservation, as the supporting silica matrix provides mechanical support during the conversion reaction, while the nanocrystals' size improves the chemical reactivity.[29,30] We rationalize that these shape-preserving properties of the nanocomposites can also be utilized for the conversion toward SnO_2.

To perform the conversion, we position the $Sn_3(OH)_2O_2/SiO_2$ nanocomposites in a tube oven that is open to air. The oven is heated to 200 °C for 3 h to induce thermal dehydration (V) and subsequently heated for 3 h at 600 °C to form SnO_2 (Figure 3A, reaction VI). XRD and EDS analyses confirm complete conversion of the nanocrystals in the nanocomposite to tetragonal SnO_2 with a grain size of 10 nm (Figure 3C,D, see Supporting Information), while electron microscopy shows excellent preservation of the microscopic features of the nanocomposite (Figure 3B). Thus, the nanocomposites retain their coral-like shape, while the nanocrystalline interior is completely converted to SnO_2.

To demonstrate the versatility and tunability of $Sn_3(OH)_2O_2/SiO_2$ nanocomposites as a precursor for functional compositions, we develop a second conversion route toward shape-controlled methylammonium tin halide perovskites ($CH_3NH_3SnX_3$, with X = Br^- or I^-). These semiconductors have a tunable band gap in the visible and near infrared spectrum, which makes them attractive for photovoltaic applications. Moreover, tin perovskites have gained attention as an environmentally friendly alternative to the widely popular lead perovskites, yet control over the 3D morphology has remained limited.[40−43] Inspired by previous conversions to lead halide perovskites,[29] we envision that conversion of $Sn_3(OH)_2O_2$ to $CH_3NH_3SnX_3$ may be achieved by reaction with methylammonium halide (CH_3NH_3X, with X = Br^- or I^-) following VII

$$Sn_3(OH)_2O_2(s) + 9CH_3NH_3X(s) \rightarrow 3CH_3NH_3SnX_3(s) + 4H_2O(g) + 6CH_3NH_2(g) \quad \text{(VII)}$$

We show the proof of principle for the conversion toward methylammonium bromide tin perovskite ($CH_3NH_3SnBr_3$). The $Sn_3(OH)_2O_2/SiO_2$ nanocomposites are placed in a tube oven, and an alumina boat containing CH_3NH_3Br is placed directly besides them. The pressure in the oven is reduced to 50 mbar, followed by a temperature increase to 120 °C for 30 min and subsequently passively cooling down the oven back to room temperature. SEM analysis shows that the initial macroscopic geometry is well preserved (Figure 4B). XRD and EDS analyses confirm that the nanocrystals in the resulting nanocomposites are completely converted to orthorhombic $CH_3NH_3SnBr_3$ with a grain size of 90 nm (see Supporting Information), as shown in Figure 4E,F. A slight roughening of the surface is observed, which may be contributed to the insertion of methyl ammonium halide and the increase in the crystal lattice from 48 to 204 $Å^3$ per tin atom. VII suggests that selecting the methylammonium halide precursor enables control over the halide moiety in the perovskite. Indeed, reaction of $Sn_3(OH)_2O_2$ nanocomposites with $CH_3NH_3SnI_3$ results in conversion to the methylammonium iodide tin perovskite with a grain size of 81 nm ($CH_3NH_3SnI_3$, Figure 4C,E,F and Supporting Information).

Control of the halide moiety during the conversion offers tunability of the band gap of the perovskite semiconductor. We characterize this band gap using photoluminescence (PL) spectroscopy. The $CH_3NH_3SnBr_3/SiO_2$ and $CH_3NH_3SnI_3/SiO_2$ nanocomposites show PL with a peak at 610 nm and 880 nm, respectively (Figure 4G), which is slightly blue-shifted compared to previously reported values, likely because of the quantum confinement of the perovskite nanocrystals in the silica matrix.[40,43,53] This confinement is consistent with the relatively broad PL peak, presumably from the size dispersion of the crystals. PL mapping furthermore shows light emission from the entire architecture, thus offering corroborative evidence of complete conversion (Figure 4D). These tin perovskites nanocomposites thus have the same photoluminescent properties as 2D tin perovskites, while offering the ability to straightforwardly program the 3D shape.

https://doi.org/10.1021/acs.cgd.1c00393
Cryst. Growth Des. XXXX, XXX, XXX−XXX

CONCLUSIONS

Here, we introduce a shape-preserving conversion from $BaCO_3/SiO_2$ to $Sn_3(OH)_2O_2/SiO_2$ nanocomposites. We propose a mechanism based on a cascade of reactions which, driven by the local pH in the reaction zone, allows this one-step cation/anion exchange. We show that the $Sn_3(OH)_2O_2$ forms can straightforwardly be converted to functional tin compositions: the semiconductor tin perovskite ($CH_3NH_3SnX_3$) and the conductor tin oxide (SnO_2), while maintaining the 3D geometry and fine features of the original $BaCO_3/SiO_2$ nanocomposite. We envisage that localized reaction zones in nanocomposites may be further exploited. Specifically, our results may enable shaping metals such as molybdenum, ruthenium, or palladium, none of which form stable carbonates, but all of which are of wide interest for their catalytic activity. Moreover, these conversion reactions could also be applied to other complex-shaped nanocomposites, such as the wide catalogue of biominerals, and create intricate patterns using lithography methods.[54] Ultimately, these findings may enable shaping metals into advanced morphologies for next-generation catalysts and optoelectronic devices.

ASSOCIATED CONTENT

Supporting Information

The Supporting Information is available free of charge at https://pubs.acs.org/doi/10.1021/acs.cgd.1c00393.

Synthesis methods and used equipment (PDF)

AUTHOR INFORMATION

Corresponding Author

Willem L. Noorduin − *AMOLF, 1098 XG Amsterdam, The Netherlands; Van 't Hoff Institute for Molecular Sciences, University of Amsterdam, 1090 GD Amsterdam, The Netherlands;* orcid.org/0000-0003-0028-2354; Email: noorduin@amolf.nl

Authors

Hans C. Hendrikse − *AMOLF, 1098 XG Amsterdam, The Netherlands*

Stivell Hémon-Charles − *AMOLF, 1098 XG Amsterdam, The Netherlands; École Polytechnique l'Université de Nantes, 44035 Nantes, France*

Lukas Helmbrecht − *AMOLF, 1098 XG Amsterdam, The Netherlands*

Eliane P. van Dam − *AMOLF, 1098 XG Amsterdam, The Netherlands;* Present Address: Department of Physical Chemistry II, Ruhr University Bochum, 44780 Bochum, Germany

Erik C. Garnett − *AMOLF, 1098 XG Amsterdam, The Netherlands;* orcid.org/0000-0002-9158-8326

Complete contact information is available at: https://pubs.acs.org/10.1021/acs.cgd.1c00393

Author Contributions

All authors have given approval to the final version of the manuscript.

Notes

The authors declare no competing financial interest.

ACKNOWLEDGMENTS

This work is part of the Vernieuwingsimpuls Vidi research program "Shaping up materials" with project number 016.Vidi.189.083, which is partly financed by the Dutch Research Council (NWO).

ABBREVIATIONSPARA

XRD	X-ray diffraction
EDS	energy-dispersive X-ray spectroscopy
SEM	scanning electron microscopy
IR	infrared spectroscopy
$BaCO_3$	witherite
$Sn_3(OH)_2O_2$	hydroromarchite
SnO	romarchite
SnO_2	cassiterite
$CH_3NH_3SnX_3$ (X = Br, I)	methylammonium tin halide perovskite
CH_3NH_3X	methylammonium halide.

REFERENCES

(1) Jiang, W.; Qu, Z.-b.; Kumar, P.; Vecchio, D.; Wang, Y.; Ma, Y.; Bahng, J. H.; Bernardino, K.; Gomes, W. R.; Colombari, F. M.; Lozada-Blanco, A.; Veksler, M.; Marino, E.; Simon, A.; Murray, C.; Muniz, S. R.; de Moura, A. F.; Kotov, N. A. Emergence of complexity in hierarchically organized chiral particles. *Science* **2020**, *368*, 642−648.

(2) Aizenberg, J.; Thanawala, M. S.; Sundar, V. C.; Morse, D. E.; Fratzl, P. Skeleton of Euplectella sp.: Structural Hierarchy from the Nanoscale to the Macroscale. *Science* **2005**, *309*, 275−278.

(3) Mann, S.; Ozin, G. A. Synthesis of inorganic materials with complex form. *Nature* **1996**, *382*, 313−318.

(4) Meldrum, F. C.; Cölfen, H. Controlling mineral morphologies and structures in biological and synthetic systems. *Chem. Rev.* **2008**, *108*, 4332−4432.

(5) Lowenstam, H. A.; Weiner, S. *On Biomineralization*; Oxford University Press: New York, NY, USA, 1989.

(6) Eder, M.; Amini, S.; Fratzl, P. Biological composites—complex structures for functional diversity. *Science* **2018**, *362*, 543−547.

(7) Begley, M. R.; Gianola, D. S.; Ray, T. R. Bridging functional nanocomposites to robust macroscale devices. *Science* **2019**, *364*, No. eaav4299.

(8) Bargardi, F. L.; Le Ferrand, H.; Libanori, R.; Studart, A. R. Bio-inspired self-shaping ceramics. *Nat. Commun.* **2016**, *7*, 1−8.

(9) Shevchenko, E. V.; Talapin, D. V.; Kotov, N. A.; O'Brien, S.; Murray, C. B. Structural diversity in binary nanoparticle superlattices. *Nature* **2006**, *439*, 55−59.

(10) Wegst, U. G. K.; Bai, H.; Saiz, E.; Tomsia, A. P.; Ritchie, R. O. Bioinspired structural materials. *Nat. Mater.* **2015**, *14*, 23−36.

(11) Whitesides, G. M.; Grzybowski, B. Self-assembly at all scales. *Science* **2002**, *295*, 2418−2421.

(12) Singh, G.; Chan, H.; Baskin, A.; Gelman, E.; Repnin, N.; Král, P.; Klajn, R. Self-assembly of magnetite nanocubes into helical superstructures. *Science* **2014**, *345*, 1149−1153.

(13) Vogel, N.; Retsch, M.; Fustin, C.-A.; Del Campo, A.; Jonas, U. Advances in Colloidal Assembly: The Design of Structure and Hierarchy in Two and Three Dimensions. *Chem. Rev.* **2015**, *115*, 6265−6311.

(14) Studart, A. R. Towards high-performance bioinspired composites. *Adv. Mater.* **2012**, *24*, 5024−5044.

(15) Terada, T.; Yamabi, S.; Imai, H. Formation process of sheets and helical forms consisting of strontium carbonate fibrous crystals with silicate. *J. Cryst. Growth* **2003**, *253*, 435−444.

(16) Malchow, A.-K.; Azhand, A.; Knoll, P.; Engel, H.; Steinbock, O. From nonlinear reaction-diffusion processes to permanent microscale structures. *Chaos* **2019**, *29*, 053129.

(17) García-Ruiz, J. M.; Amorós, J. L. Morphological aspects of some symmetrical crystal aggregates grown by silica gel technique. *J. Cryst. Growth* **1981**, *55*, 379−383.
(18) García-Ruiz, J. M.; Hyde, S. T.; Carnerup, A. M.; Christy, A. G.; Van Kranendonk, M. J.; Welham, N. J. Self-assembled silica-carbonate structures and detection of ancient microfossils. *Science* **2003**, *302*, 1194−1197.
(19) Bittarello, E.; Aquilano, D. Self-assembled nanocrystals of barium carbonate in biomineral-like structures. *Eur. J. Mineral.* **2007**, *19*, 345−351.
(20) Kellermeier, M.; Cölfen, H.; García-Ruiz, J. M. Silica biomorphs: Complex biomimetic hybrid materials from "Sand and Chalk". *Eur. J. Inorg. Chem.* **2012**, *2012*, 5123−5144.
(21) García-Ruiz, J. M.; Melero-García, E.; Hyde, S. T. Morphogenesis of Self-Assembled Nanocrystalline Materials of Barium Carbonate and Silica. *Science* **2009**, *323*, 362−365.
(22) Noorduin, W. L.; Grinthal, A.; Mahadevan, L.; Aizenberg, J. Rationally designed complex, hierarchical microarchitectures. *Science* **2013**, *340*, 832−837.
(23) Kaplan, C. N.; Noorduin, W. L.; Li, L.; Sadza, R.; Folkertsma, L.; Aizenberg, J.; Mahadevan, L. Controlled growth and form of precipitating microsculptures. *Science* **2017**, *355*, 1395−1399.
(24) Opel, J.; Unglaube, N.; Wörner, M.; Kellermeier, M.; Cölfen, H.; García-Ruiz, J. M. Hybrid Biomimetic Materials from Silica/Carbonate Biomorphs. *Crystals* **2019**, *9*, 157.
(25) Nakouzi, E.; Steinbock, O. Self-organization in precipitation reactions far from the equilibrium. *Sci. Adv.* **2016**, *2*, No. e1601144.
(26) Helmbrecht, L.; Tan, M.; Röhrich, R.; Bistervels, M. H.; Ortiz Kessels, B.; Koenderink, A. F.; Kahr, B.; Noorduin, W. L. *Adv. Funct. Mater.* **2019**, *30*, 1908218.
(27) Opel, J.; Wimmer, F. P.; Kellermeier, M.; Cölfen, H. Functionalisation of silica-carbonate biomorphs. *Nanoscale Horiz.* **2016**, *1*, 144−149.
(28) Opel, J.; Brunner, J.; Zimmermanns, R.; Steegmans, T.; Sturm, E.; Kellermeier, M.; Cölfen, H.; García-Ruiz, J. M. Symbiosis of Silica Biomorphs and Magnetite Mesocrystals. *Adv. Funct. Mater.* **2019**, *29*, 1902047.
(29) Holtus, T.; Helmbrecht, L.; Hendrikse, H. C.; Baglai, I.; Meuret, S.; Adhyaksa, G. W. P.; Garnett, E. C.; Noorduin, W. L. Shape-preserving transformation of carbonate minerals into lead halide perovskite semiconductors based on ion exchange/insertion reactions. *Nat. Chem.* **2018**, *10*, 740−745.
(30) Hendrikse, H. C.; Weijden, A.; Ronda-Lloret, M.; Yang, T.; Bliem, R.; Shiju, N. R.; Hecke, M.; Li, L.; Noorduin, W. L. Shape-preserving chemical conversion of architected nanocomposites. *Adv. Mater.* **2020**, *32*, 2003999.
(31) De Trizio, L.; Manna, L. Forging colloidal nanostructures via cation exchange reactions. *Chem. Rev.* **2016**, *116*, 10852−10887.
(32) Beberwyck, B. J.; Surendranath, Y.; Alivisatos, A. P. Cation exchange: A versatile tool for nanomaterials synthesis. *J. Phys. Chem. C* **2013**, *117*, 19759−19770.
(33) Backhaus-Ricoult, M. Solid-State Reactivity at Heterophase Interfaces. *Annu. Rev. Mater. Res.* **2003**, *33*, 55−90.
(34) Putnis, A. Why mineral interfaces matter. *Science* **2014**, *343*, 1441−1442.
(35) Lothenbach, B.; Ochs, M.; Wanner, H.; Yui, M. *Thermodynamic Data for the Speciation and Solubility of Pd, Pb, Sn, Sb, Nb and Bi in Aqueous Solution*; Japan Nucl. Cycle Dev. Inst., 2004; pp 1−356.
(36) Chen, Y.; Kanan, M. W. Tin oxide dependence of the CO_2 reduction efficiency on tin electrodes and enhanced activity for tin/tin oxide thin-film catalysts. *J. Am. Chem. Soc.* **2012**, *134*, 1986−1989.
(37) Barsan, N.; Weimar, U. Conduction model of metal oxide gas sensors. *J. Electroceram.* **2001**, *7*, 143−167.
(38) Feaster, J. T.; Shi, C.; Cave, E. R.; Hatsukade, T.; Abram, D. N.; Kuhl, K. P.; Hahn, C.; Nørskov, J. K.; Jaramillo, T. F. Understanding Selectivity for the Electrochemical Reduction of Carbon Dioxide to Formic Acid and Carbon Monoxide on Metal Electrodes. *ACS Catal.* **2017**, *7*, 4822−4827.
(39) Chen, J. S.; Lou, X. W. D. SnO_2-based nanomaterials: Synthesis and application in lithium-ion batteries. *Small* **2013**, *9*, 1877−1893.
(40) Konstantakou, M.; Stergiopoulos, T. A critical review on tin halide perovskite solar cells. *J. Mater. Chem. A* **2017**, *5*, 11518−11549.
(41) Snaith, H. J. Perovskites: The Emergence of a New Era for Low-Cost, High-Efficiency Solar Cells. *J. Phys. Chem. Lett.* **2013**, *4*, 3623−3630.
(42) Stoumpos, C. C.; Malliakas, C. D.; Kanatzidis, M. G. Semiconducting tin and lead iodide perovskites with organic cations: Phase transitions, high mobilities, and near-infrared photoluminescent properties. *Inorg. Chem.* **2013**, *52*, 9019−9038.
(43) Hao, F.; Stoumpos, C. C.; Cao, D. H.; Chang, R. P. H.; Kanatzidis, M. G. Lead-free solid-state organic-inorganic halide perovskite solar cells. *Nat. Photonics* **2014**, *8*, 489−494.
(44) The X-Ray diffractogram suggests that part of the tin composite is amorphous.
(45) Knoll, P.; Steinbock, O. Nanodot-to-Rod Transition and Particle Attachment in Self-Organized Polycrystalline Aggregates. *Cryst. Growth Des.* **2019**, *19*, 4218−4223.
(46) Chen, X.; Grandbois, M. In situ Raman spectroscopic observation of sequential hydrolysis of stannous chloride to abhurite, hydroromarchite, and romarchite. *J. Raman Spectrosc.* **2013**, *44*, 501−506.
(47) Edwards, R.; Gillard, R. D.; Williams, P. A. The stabilities of secondary tin minerals: abhurite and its relationships to Sn(II) and Sn(IV) oxides and oxyhydroxides. *Mineral. Mag.* **1992**, *56*, 221−226.
(48) Pettine, M.; Millero, F. J.; Macchi, G. Hydrolysis of Tin(II) in Aqueous Solutions. *Anal. Chem.* **1981**, *53*, 1039−1043.
(49) It should be noted that in the absence of a base abhurite rather than hydroromarchite forms after ca. 30 minutes in the reaction mixture following: $21Sn^{2+}(aq) + 16Cl^{-}(aq) + 20H_2O(l) \rightarrow Sn_{21}Cl_{16}(OH)_{14}O_6(s) + 26H^{+}(aq)$.
(50) Kitabayashi, S.; Koga, N. Thermal Decomposition of Tin(II) Oxyhydroxide and Subsequent Oxidation in Air: Kinetic Deconvolution of Overlapping Heterogeneous Processes. *J. Phys. Chem. C* **2015**, *119*, 16188−16199.
(51) Wongsaprom, K.; Bornphotsawatkun, R.-a.; Swatsitang, E. Synthesis and characterization of tin oxide (SnO_2) nanocrystalline powders by a simple modified sol-gel route. *Appl. Phys. A: Mater. Sci. Process.* **2014**, *114*, 373−379.
(52) Alcántara, R.; Madrigal, F. F.; Lavela, P.; Pérez-Vicente, C.; Tirado, J. Tin oxalate as a precursor of tin dioxide and electrode materials for lithium-ion batteries. *J. Solid State Electrochem.* **2001**, *6*, 55−62.
(53) Walters, G.; Wei, M.; Voznyy, O.; Quintero-Bermudez, R.; Kiani, A.; Smilgies, D.-M.; Munir, R.; Amassian, A.; Hoogland, S.; Sargent, E. The quantum-confined Stark effect in layered hybrid perovskites mediated by orientational polarizability of confined dipoles. *Nat. Commun.* **2018**, *9*, 4214.
(54) Helmbrecht, L.; Futscher, M. H.; Muscarella, L. A.; Ehrler, B.; Noorduin, W. L. Ion Exchange Lithography: Localized Ion Exchange Reactions for Spatial Patterning of Perovskite Semiconductors and Insulators. *Adv. Mater.* **2021**, *33*, 2005291.

https://doi.org/10.1021/acs.cgd.1c00393
Cryst. Growth Des. XXXX, XXX, XXX−XXX